

Epitaxial Growth and Electronic Properties of Single- and Few-Layer FeBr₂ on Bi(111)

Shigemi Terakawa,* Shinichiro Hatta, Hiroshi Okuyama, and Tetsuya Aruga

Cite This: *J. Phys. Chem. C* 2023, 127, 14898–14905

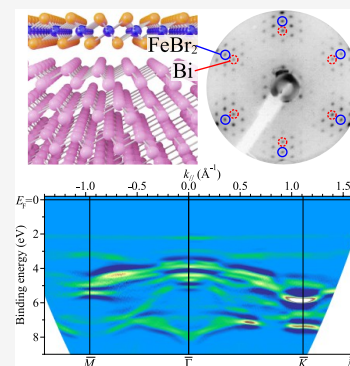
Read Online

ACCESS |

Metrics & More

Article Recommendations

ABSTRACT: Magnetic van der Waals (vdW) materials have attracted considerable attention in recent years because of their future spintronics applications. 3d Transition metal dihalides are a promising class of materials to realize two-dimensional vdW magnets with intriguing magnetic and electronic properties. We report the epitaxial growth of (0001)-oriented FeBr₂ films from the monolayer by molecular beam epitaxy on the Bi(111) surface. The atomic structure was confirmed to be identical to that of the bulk FeBr₂ crystal by dynamical low-energy electron diffraction analysis. Angle-resolved photoelectron spectroscopy revealed that the topmost valence band composed of Fe 3d orbitals is located at 2.2 eV below the Fermi level, showing that the FeBr₂ films are insulating down to the monolayer.



INTRODUCTION

Since the discovery of graphene and its astonishing physical properties,^{1,2} two-dimensional (2D) van der Waals (vdW) materials have been attracting extensive attention. Magnetic vdW materials are of particular interest as they are promising for future spintronic applications.^{3–9} Furthermore, the vdW magnets can be used to fabricate heterostructures with various materials including topological insulators and superconductors to exploit magnetic proximity effects, which leads to the realization of novel quantum phases such as the topological superconductivity and the quantum anomalous Hall effect.^{10–12} Recent experimental studies found ferromagnetic order in atomically thin vdW materials such as CrI₃,¹³ CrBr₃,¹⁴ CrCl₃,¹⁵ Cr₂Ge₂Te₆,¹⁶ and Fe₃GeTe₂.¹⁷ 3d Transition metal dihalides are also good candidates for realizing 2D magnets because many of them have layered structure in bulk and exhibit a rich variety of magnetic states.¹⁸ In theoretical calculations, their monolayers exhibit energetically and dynamically stable magnetic ground states depending on their component metal and halogen atoms. Experimental research of their monolayers has only just begun and their physical properties have been experimentally investigated in only a few transition metal dihalides including FeCl₂, NiBr₂, and NiI₂.^{19–23}

FeBr₂ has a CdI₂-type layered structure, where Br–Fe–Br triple layers (TLs) with hexagonal 1T configuration are stacked along the [0001] axis with weak vdW-type interaction. The monolayer FeBr₂ corresponds to the 1-TL film. Bulk FeBr₂ is an Ising-type antiferromagnetic insulator with a Néel temperature (T_N) of 14.2 K.^{24,25} The magnetic moments on the Fe

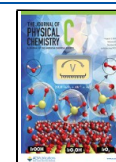
atoms are ferromagnetically aligned perpendicular to the (0001) plane in each TL, and they are antiferromagnetically coupled between adjacent TLs. Many theoretical works commonly predict that the in-plane ferromagnetic order remains in the 1-TL film of FeBr₂ and isomorphous FeCl₂.^{26–31} On the other hand, the calculated electronic structures are controversial: some say that they are half-metallic^{26–28} and the others say insulating.^{30–32} Therefore, it is important to establish a method to fabricate ultrathin FeBr₂ films and experimentally reveal the electronic properties. Moreover, it is interesting to investigate the effect of the interaction with the substrate on the physical properties of the films.

In this study, we report the growth of high-quality ultrathin FeBr₂ films by molecular beam epitaxy (MBE) on the hexagonal Bi(111) surface. Low-energy electron diffraction (LEED) experiments and dynamical analysis showed that the (0001)-oriented FeBr₂ films are epitaxially grown and that the atomic structure is identical to that of bulk FeBr₂. The 1-TL film shows sharp satellite spots attributed to a moiré pattern due to lattice matching of FeBr₂(0001) to Bi(111) in a ratio of 13:11. Angle-resolved photoelectron spectroscopy (ARPES) measurements revealed that the FeBr₂ films have insulating

Received: April 1, 2023

Revised: June 2, 2023

Published: July 19, 2023



electronic structure down to monolayer with the topmost valence band composed of Fe 3d located at 2.2 eV below the Fermi level. The difference between multilayer and monolayer was found as a significant narrowing of the Br 4p bands, which is attributed to the disappearance of Br–Br interlayer interaction in the monolayer.

METHODS

All experiments were carried out in an ultrahigh vacuum (UHV) chamber with a base pressure of $\sim 1 \times 10^{-10}$ Torr. Bi(111) substrates were prepared as a single-crystalline film grown on Si(111). Si(111) substrates (n-type) were cleaned by direct-current heating at 1500 K. Bi was deposited on the clean Si(111) (7×7) surface at room temperature (RT) at a thickness of 6 nm, and then, the Bi films were annealed at around 400 K to obtain uniform (111)-oriented terraces as reported in the literature.^{33,34} FeBr₂ powder in a tantalum crucible was heated at 620 K and deposited onto the Bi(111) surface at RT followed by annealing at 490 K for half a minute. The thickness of FeBr₂ was measured by a quartz microbalance.

LEED and ARPES measurements were conducted in situ with LEED optics (OCI BDL600) and a hemispherical electron energy analyzer (Scienta R3000), respectively. ARPES data were obtained with monochromatized He I α and He II α radiation ($h\nu = 21.2$ and 40.8 eV, respectively). The Fermi level was determined from a Fermi edge measured on a tantalum foil in contact with the samples.

Density functional theory (DFT) calculations were performed using the projector-augmented-wave (PAW) method^{35,36} implemented in the Vienna Ab initio Simulation Package (VASP).^{37–39} The atomic positions were fully optimized using the optB86b-vdW functional,⁴⁰ and the band structures were calculated using the spin-polarized Perdew–Burke–Ernzerhof (PBE) functional.⁴¹ The kinetic energy cutoff was set to 475 eV. The Γ -centered $11 \times 11 \times 1$ k -point mesh was used to sample the Brillouin zones (BZs).

RESULTS AND DISCUSSION

Figure 1a shows a LEED pattern of the Bi(111) film. The measured in-plane lattice constant of 4.48 Å agrees with the previously reported value.³³ The threefold LEED pattern reflects the twin-free structure of the Bi film. Sharp spots and low background intensity indicate the high quality of the Bi film. Figure 1b shows a LEED pattern of the FeBr₂ film at a thickness of 4.0 TL. The locations of the Bi(111) spots are

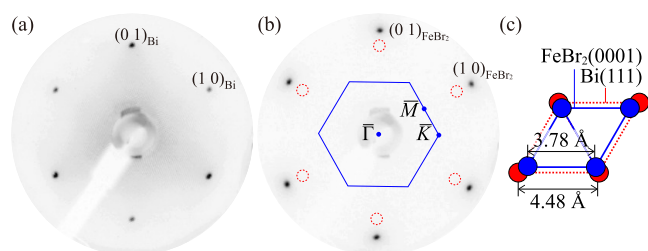


Figure 1. LEED patterns of the (a) 6-nm Bi(111) film and (b) 4.0-TL FeBr₂(0001) film at RT ($E_p = 46$ eV). The red dotted circles in panel (b) indicate the positions of the Bi(111) spots obtained from panel (a). The blue solid hexagon in panel (b) represents the first Brillouin zone corresponding to FeBr₂(0001). (c) The unit cells of FeBr₂(0001) (blue solid lines) and Bi(111) (red dotted lines).

indicated by the red dotted circles in Figure 1b. The six spots of the FeBr₂ film are located outside of the Bi(111) spots. The in-plane lattice constant was measured to be 3.78 ± 0.01 Å, which agrees with the lattice constant of the bulk FeBr₂(0001) plane (3.776 Å).⁴² The corresponding unit cells in real space are displayed in Figure 1c. The LEED patterns show the epitaxial growth of FeBr₂(0001) on Bi(111), where the unit vectors of FeBr₂(0001) are parallel to those of Bi(111). The sharpness of the FeBr₂ spots is comparable to that of the Bi(111) spots. In contrast to the threefold rotational symmetry of the Bi pattern, the pattern of the FeBr₂ film exhibits six-fold symmetry irrespective of incident electron energy. Therefore, the FeBr₂ film consists of twin domains whose orientations are rotated by 180° with respect to each other.

In order to determine the atomic structure of the FeBr₂ film, we performed LEED I – V measurements for the 4.0-TL film. The thickness (2.5 nm) is large enough to neglect the influence of the FeBr₂/Bi interface. LEED patterns at 60–500 eV were recorded in increments of 1 eV at 80 K. An image at a high energy of 330 eV is present in the inset of Figure 3a. The I – V curves were normalized by the primary beam current and averaged over the symmetry equivalent beams. The total energy range was 1742 eV. We examined 12 structure models in Figure 2. The models are all possible stacking sequences of

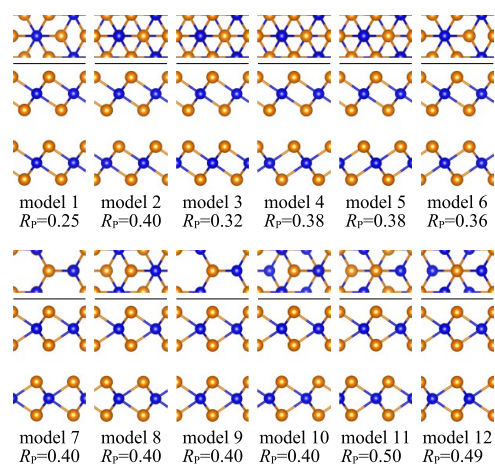


Figure 2. Top and side views of examined structural models and the R_p values for the FeBr₂ film. The blue and yellow balls indicate the Fe and Br atoms, respectively. The atomic structures were visualized using VESTA.⁴³

TLs with 1T structure for models 1–6 and 1H structure for models 7–12 with threefold rotational symmetry. Model 1 is the CdI₂ structure identical to bulk FeBr₂. We used the Barbieri–Van Hove symmetrized automated tensor LEED (SATLEED) package for full dynamical calculations⁴⁴ and took the coexistence of the twin domains with different orientations into consideration. The calculated and experimental I – V curves were compared by Pendry’s reliability factor (R_p).⁴⁵ For initial screening, we used phase shifts up to $l_{\max} = 8$, and then, it was increased up to $l_{\max} = 12$ in the further optimization of atomic positions in the topmost six atomic layers (2 TLs). The errors of the structural parameters were evaluated with the Pendry RR function.⁴⁵ The calculated R_p values for all of the models are presented in Figure 2. Model 1 shows a notably small R_p value of 0.25 and the variance is 0.04. The other models can be excluded because their R_p values are larger than 0.29.

We further optimized the structural parameters and Debye temperatures of the best model. The optimum Debye temperatures were 180 K for the topmost Br atoms, 210 K for the Fe atoms, and 260 K for Br atoms beneath. We finally obtained the minimum R_p value of 0.15. The calculated $I-V$ curves (the dotted curves in Figure 3a) are in excellent

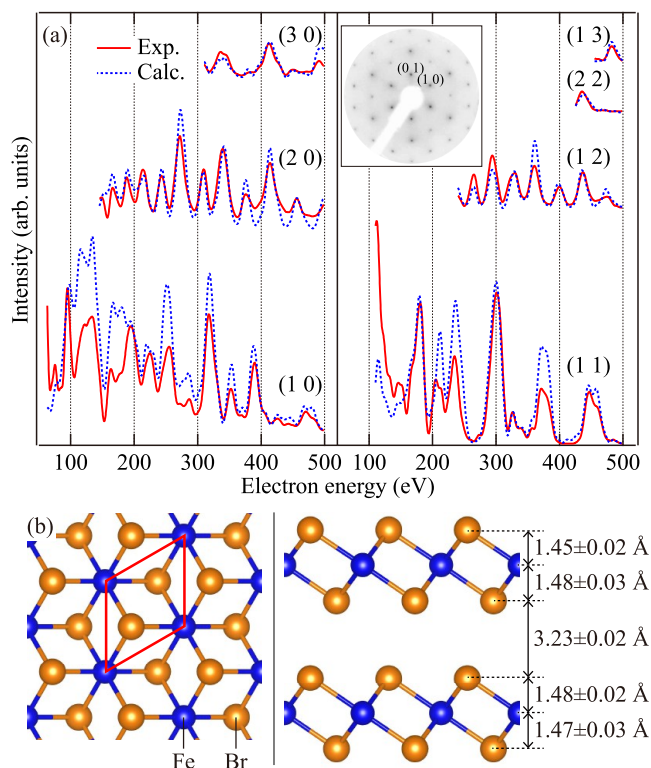


Figure 3. (a) Experimental (solid) and calculated (dotted) LEED $I-V$ curves for the optimized structure. The inset shows the LEED pattern of the 4.0-TL FeBr_2 film at 80 K ($E_p = 330$ eV). (b) Top (left) and side (right) views of the optimized FeBr_2 structure. The red solid parallelogram represents the unit cell of the $\text{FeBr}_2(0001)$ plane. The blue and yellow balls indicate the Fe and Br atoms, respectively. The atomic structure was visualized using VESTA.⁴³

agreement with the experimental curves (the solid curves). The optimized structure is shown in Figure 3b with the structural

parameters, which agree well with those in the bulk: 1.483 Å for Br–Fe and 3.262 Å for Br–Br.⁴²

Figure 4a shows an ARPES band map of the 4.0-TL FeBr_2 film at 30 K (see the BZ in Figure 1b). For better identification of band features with a large difference in intensity, the second derivative of energy distribution curves (d^2I/dE^2) is plotted in a color scale shown at the bottom. We found little difference in spectra measured at RT and 30 K except for thermal broadening at RT. The observed valence band structure of FeBr_2 is understood by dividing it into two parts above and below 3.7 eV. This is intuitively indicated by a considerable difference in photoelectron intensity between the two regions, as shown in the raw ARPES data (Figure 4b) and its angle-integrated spectrum (the red solid curve in Figure 4d). In the lower region, many bands mainly derived from Br 4p orbitals disperse strongly upward or downward from $\bar{\Gamma}$ and show backfolding according to the BZ of $\text{FeBr}_2(0001)$. In contrast, the dispersions of the two bands in the upper region are quite weak. Especially, the upper band at 2.2 eV is nearly flat. The small dispersion of the upper two bands indicates that they have large contributions of localized Fe 3d orbitals.

The photoemission cross section for Fe 3d is increased by increasing photon energy from 21.2 eV (He I α) to 40.8 eV (He II α).⁴⁶ Figure 4b,c presents the ARPES data as plots of photoemission intensity measured with He I α and He II α , respectively. Figure 4d shows the comparison of the angle-integrated energy distribution curves with He I α (red solid curve) and He II α (blue dotted curve). These spectra were normalized with respect to the maximum intensity. Although the band dispersions measured with the two photon energies generally agree with each other, the two upper bands at 2.2 and 3.2 eV show a drastic increase with He II α , which supports the above assignment of the two bands as the Fe 3d bands. In addition, the band at around 5 eV at \bar{K} is also enhanced with He II α , indicating that there are Fe 3d-derived bands as well as Br 4p bands in the lower energy region. It is noted that there is no state at the Fermi level even in the integrated spectra both with He I α and He II α . This shows that the 4.0-TL film is insulating, and the valence band maximum is located at 2.2 eV below the Fermi level.

The above results indicate that the electronic properties of the $\text{FeBr}_2(0001)$ film at a thickness of 4.0 TL (2.5 nm) are consistent with the insulating nature of bulk FeBr_2 . It is more

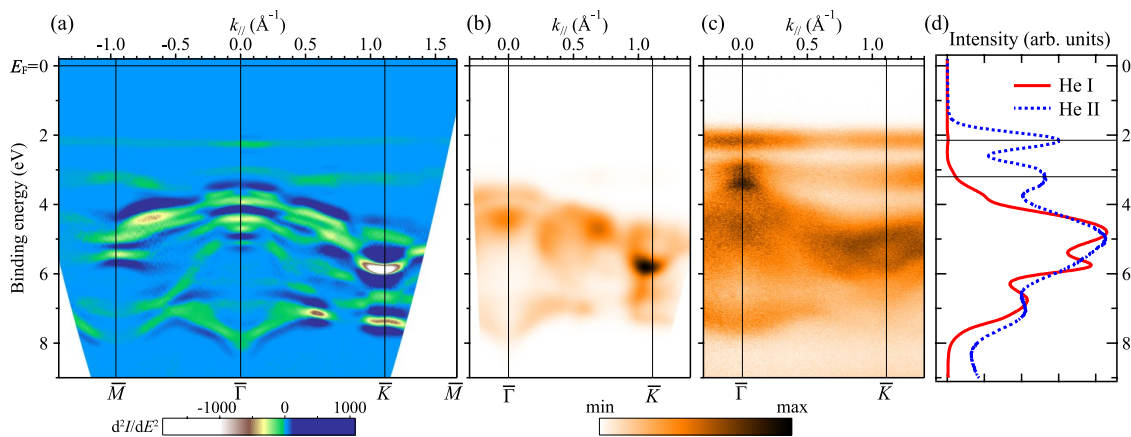


Figure 4. (a) Second derivative of the ARPES band map of the 4.0-TL FeBr_2 film at 30 K along $\bar{M}-\bar{\Gamma}-\bar{K}-\bar{M}$ measured with He I α . ARPES band maps of the 4.0-TL FeBr_2 film at RT along $\bar{\Gamma}-\bar{K}$ measured with (b) He I α ($h\nu = 21.2$ eV) and (c) He II α ($h\nu = 40.8$ eV). (d) Angle-integrated photoelectron spectra of panel (b) red solid curve and panel (c) blue dotted curve.

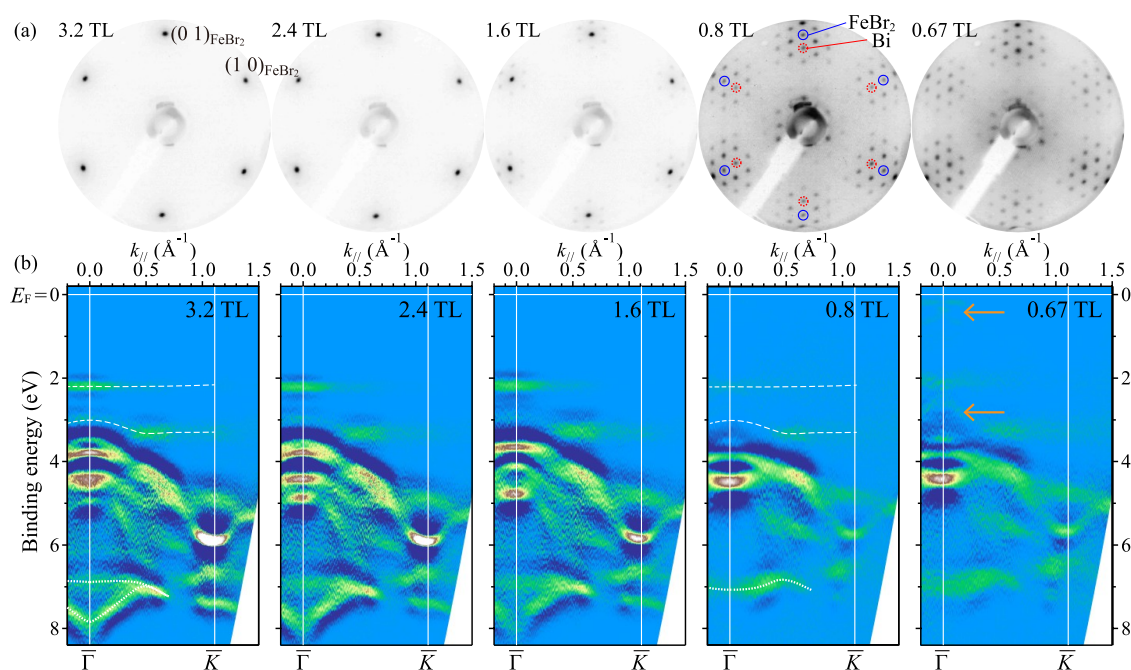


Figure 5. Thickness dependence of the (a) LEED patterns and (b) ARPES band maps along $\bar{\Gamma}-\bar{K}$ of the FeBr_2 films with thicknesses of 3.2, 2.4, 1.6, 0.8, and 0.67 TL measured at RT. The red dotted and blue solid circles in the 0.8-TL pattern indicate the spots corresponding to $\text{Bi}(111)$ and $\text{FeBr}_2(0001)$, respectively. The ARPES data were obtained using He I α . The arrows on the band map at 0.67 TL indicate the bands from the $\text{Bi}(111)$ substrate.

interesting to investigate whether the film thickness can decrease down to a single TL while maintaining crystal quality and how the electronic structure changes with the thickness. In LEED patterns for thinner films, the influence of the FeBr_2/Bi interface was found below 2 TL. Figure 5a shows the LEED patterns of the FeBr_2 films with thicknesses of 3.2, 2.4, 1.6, 0.8, and 0.67 TL. Thickness-dependent change in the positions of the FeBr_2 spots was within the error of the measurement (0.01 \AA^{-1}). With decreasing thickness, satellite spots surrounding each of the $\text{FeBr}_2(0001)$ spots appeared and became intense. The intensity of the satellite spots was maximized at 0.8 TL. The positions of the satellite spots just inside the $\text{FeBr}_2(0001)$ spots, which are indicated by the red dotted circles in Figure 5a, were found to coincide with those of the $\text{Bi}(111)$ spots (Figure 1a). These spots are sharp even at 1 TL, indicating that the domain size of the FeBr_2 film is significantly larger than the electron coherence length of typically 150 \AA .

Here we focus on the origin of the multiple satellite spots. We measured the distances between adjacent $\text{Bi}(111)$ (1×1) spots (the red dotted circles) and $\text{FeBr}_2(0001)$ (1×1) spots (the blue solid circles) for the 0.8-TL LEED pattern (Figure 5a). The average distance was $0.29 \pm 0.01 \text{ \AA}^{-1}$ and the ratios to the length of the unit reciprocal vectors corresponding to $\text{FeBr}_2(0001)$ and $\text{Bi}(111)$ were 6.5 and 5.5, respectively. Therefore, the observed complex pattern is not attributed to a hexagonal superlattice described with integer coefficients with respect to the unit vectors of $\text{FeBr}_2(0001)$ and $\text{Bi}(111)$. Nevertheless, the values of 6.5 and 5.5 suggest the lattice coincidence between $13 \times a_{\text{FeBr}_2}$ and $11 \times a_{\text{Bi}}$. The in-plane lattice constants of $a_{\text{FeBr}_2} = 3.78 \text{ \AA}$ and $a_{\text{Bi}} = 4.48 \text{ \AA}$ show only a small mismatch of 0.3%. The integer difference of 2 between the coefficients 13 and 11 yields a configuration change as “in-phase \rightarrow out-of-phase \rightarrow quasi-in-phase \rightarrow out-of-phase \rightarrow in-phase” along on the lines parallel to unit vectors as shown in

the schematic model of Figure 6. As the in-phase and quasi-in-phase configurations modulate atomic positions in a similar

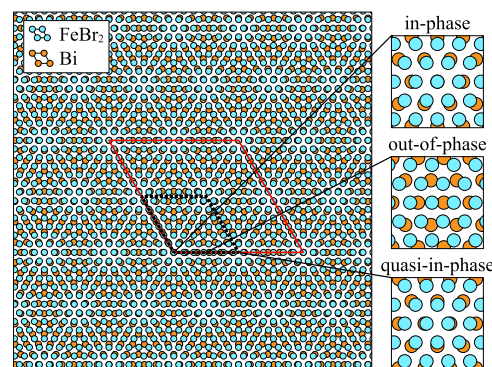


Figure 6. Schematic model of the $\text{FeBr}_2(0001)$ and $\text{Bi}(111)$ lattices when assuming the commensurate structure of $(13 \times 13)_{\text{FeBr}_2} = (11 \times 11)_{\text{Bi}}$. The blue and orange circles represent the lattice points of $\text{FeBr}_2(0001)$ and $\text{Bi}(111)$, respectively. The red solid and black dotted parallelograms represent the superlattice of $(13 \times 13)_{\text{FeBr}_2} = (11 \times 11)_{\text{Bi}}$ and the quasi-superlattice of $(6.5 \times 6.5)_{\text{FeBr}_2} = (5.5 \times 5.5)_{\text{Bi}}$, respectively. The in-phase, out-of-phase, and quasi-in-phase configurations are enlarged on the right.

way, the diffraction pattern should be characterized by the half period of $13 \times a_{\text{FeBr}_2}$, namely, 6.5 with respect to $\text{FeBr}_2(0001)$, and likewise, 5.5 with respect to $\text{Bi}(111)$, indicated by the black dotted parallelogram in Figure 6. These values are consistent with the LEED observation. Such modulation is expected to be observed by scanning tunneling microscopy (STM) as a moiré pattern. Note that it is still unknown whether the small mismatch of 0.3% causes relaxation in the $\text{Bi}(111)$ or 1-TL FeBr_2 structure although the LEED pattern

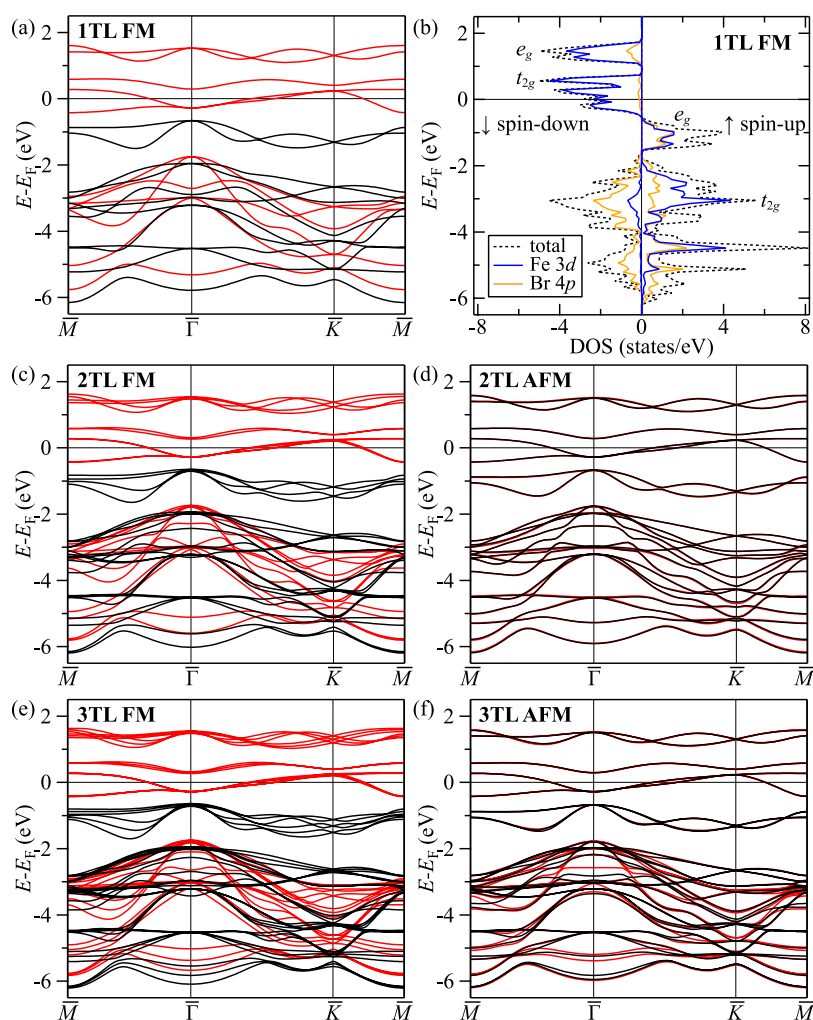


Figure 7. Calculated band structures of FeBr₂ with different thicknesses and magnetic states: (a) 1-TL FM, (c) 2-TL FM, (d) 2-TL AFM, (e) 3-TL FM, and (f) 3-TL AFM. The black and red lines represent the spin-up and spin-down channels, respectively. (b) Calculated total DOS (the black dashed lines) and partial DOS (the blue and orange solid lines) of 1-TL FeBr₂ with FM state.

suggests a commensurate superstructure of $(13 \times 13)_{\text{FeBr}_2} = (11 \times 11)_{\text{Bi}}$. This is because the lattice relaxation of 0.3% ($\sim 0.01 \text{ \AA}$) is within the uncertainty of the LEED measurement.

Figure 5b shows ARPES band maps of the FeBr₂ films for the same thicknesses set in panel (a). We first describe the band structure change from 3.2 to 0.8 TL. For the Br 4p bands, thickness-dependent changes were clearly found near $\bar{\Gamma}$; the top part of the Br band was gradually flattened and shifted downward from 3.2 to 0.8 TL, and the bottom part showed the disappearance of the lowest band at around 8 eV from 1.6 to 0.8 TL as indicated by the white dotted curves. The remarkable narrowing of the Br bandwidth from multilayer to monolayer is related to the disappearance of the Br–Br electronic interaction between adjacent TLs. In contrast, thickness-dependent change was negligible for the two Fe 3d bands indicated by the white dashed curves. Furthermore, no new feature was observed near the Fermi level, showing that the 1-TL FeBr₂ film is insulating as well as the thicker films.

When the thickness was decreased below 0.8 TL, new band features were seen near $\bar{\Gamma}$ at 0.0–0.9 and 2.2–3.1 eV as indicated by the orange arrows in the 0.67-TL band map in Figure 5b. These bands correspond to the ones from the Bi(111) substrate. Except for the Bi bands, no change was observed between the 0.8-TL and 0.67-TL films. The stronger

Bi(111) band features below 0.8 TL and the highest intensity of the LEED satellite spots at 0.8 TL suggest that the monolayer is completed at the 0.8-TL thickness and that the thickness is slightly underestimated. Considering that the deposition rate was determined by the thickness measured in a thick-film regime of FeBr₂ with a quartz microbalance, the underestimation might be attributed to a higher sticking probability of FeBr₂ on Bi compared to FeBr₂ on FeBr₂. The overall band feature of FeBr₂ at 0.8–3.2 TL was as sharp as the 4.0-TL film. The sharp moiré LEED pattern and ARPES band structure indicate successful growth of the epitaxial FeBr₂ films from the monolayer. Nevertheless, the observed band structure did not show distinct thickness dependence such as the increase of the number of valence bands with the number of TL. Thus, layer-by-layer growth on multi-TL films has not been confirmed and real-space measurements using, for example, STM is required.

In order to gain more insight into the magnetic and electronic properties of the ultrathin FeBr₂ films, we performed first-principles total energy and band structure calculations for free-standing FeBr₂ films with thicknesses of 1, 2, and 3 TL. Previous theoretical works predict that 1-TL FeBr₂ has a ferromagnetic (FM) order with the high-spin d^6 configuration of the Fe²⁺ ion.^{27,30} Here, we examined the interlayer magnetic

couplings. We compared the total energies of 2 TL, 3 TL, and bulk FeBr₂ with FM and antiferromagnetic (AFM) interlayer couplings while preserving the intralayer FM coupling and found that the AFM coupling is more favorable than the FM coupling for all of the structures. The total energy differences between the AFM and FM states per TL–TL interface were calculated to be -15.0 , -8.2 , and -9.4 meV for 2 TL, 3 TL, and bulk FeBr₂, respectively. The result suggests that the AFM stacking of the bulk FeBr₂ persists down to 2 TL with almost the same or even higher transition temperature. The calculated magnetic moments per unit cell are $4.16\mu_{\text{B}}$ in all of the FeBr₂ structures, which are in good agreement with the experimental value of $4.4\mu_{\text{B}}$ for bulk FeBr₂.²⁴

We next calculated the band structure for 1 TL, 2 TL, and 3 TL FeBr₂ with FM and AFM configurations. Figure 7a,b shows the spin-resolved band structure and density of states (DOS) of 1-TL FeBr₂ in the FM state, respectively. The valence bands are mainly composed of Fe 3d and Br 4p orbitals. The partial DOS for Fe 3d and Br 4p shows a good agreement with that previously calculated for bulk FeBr₂.⁴⁷ The Fe 3d orbitals are split into two higher-lying e_{g} states and three lower-lying $t_{2\text{g}}$ states by the octahedral crystal field formed by the six neighboring Br atoms. For the spin-down channel (the red lines in Figure 7a and the left part of Figure 7b), the Fe 3d and Br 4p bands are energetically separated. The Br 4p orbitals form highly dispersive bands below the Fermi level and the Fe 3d e_{g} and $t_{2\text{g}}$ orbitals form unoccupied and partially occupied weakly dispersive bands, respectively. The Fe 3d states in the spin-up channel (the black lines in Figure 7a and the right part of Figure 7b) are fully occupied and located in the same energy range as the Br 4p states. The e_{g} bands are located at around -1 eV and the $t_{2\text{g}}$ bands are not clearly distinguishable from the dispersive Br 4p bands. The Fe 3d and Br 4p contributions to the band structures of 2-TL and 3-TL FeBr₂ can be understood in the same way.

We compare the calculated band structures with the experimental ones. Although the measurement temperature is higher than the bulk magnetic transition temperature of 14.2 K,^{24,25} at which the magnetic long-range order disappears, the short-range order still exists with a finite correlation length and the measured states are considered to be close to the mixing states between the interlayer AFM and FM states. Indeed, the band structures calculated for the FM or AFM states agree much better with the experimental ones than those calculated for the nonmagnetic states. Such agreement between band structures calculated for FM states and experimental ones above magnetic transition temperatures is also reported for bulk vdW ferromagnets such as VI₃, CrI₃, and Cr₂Ge₂Te₆.^{48–50}

Thickness-dependent change of the band structures is mainly found on the bottom bands located in the energy range of -5 to -6 eV at $\bar{\Gamma}$. These bands are composed of Br 4p_z orbitals pointing in the out-of-plane direction and are significantly affected by the TL–TL interface. This is consistent with the experimental result that the pronounced change from monolayer to multilayer is observed in the bottom bands at $\bar{\Gamma}$. For monolayer FeBr₂, the band is observed as a single band (see the 0.8-TL panel of Figure 5b), while there are two spin-split bands in the calculation. This discrepancy can be understood by considering that our measurement temperature is higher than the magnetic transition temperature and that the width of the observed band itself (0.5 eV) is comparable to the calculated splitting of 0.47 eV. For thicker FeBr₂, the bands are observed as two bands separated by 0.9

eV (see the white dotted lines in the left panel of Figure 5b). In the calculation for the FM states, the bandwidth increases to 0.91 eV (2 TL) and 1.07 eV (3 TL) because of the formation of new states by the hybridization between the states on different TLs with each spin orientation. On the other hand, in the calculation for the AFM states, the spin on each TL has an opposite direction and thus the hybridization between the states on different TLs is much weaker. As a result, the number of almost energetically degenerate bands is increased with two center energies at -5 and -6 eV, and the bandwidth changes to 0.64 eV (2 TL) and 0.78 eV (3 TL). The calculation for the AFM states reproduces the experimental observation showing two separate bands regardless of TL number, while the values of the bandwidth calculated for the FM states are closer to the experimental ones. It should also be noted that the downward shift and flattening of the upper Br 4p bands observed by ARPES are not reproduced by our calculation, implying the influence of the Bi(111) surface in the thinner films.

Finally, we describe the Fe 3d bands involved in the magnetic properties of FeBr₂. In some theoretical studies^{26–28} as well as our calculations, the Fe 3d band of FeBr₂ is predicted to be metallic. In our ARPES measurements, the topmost Fe 3d band was observed at 2.2 eV below the Fermi level down to the monolayer. Compared to the ARPES results in Figures 4 and 5 with the calculated band structures in Figure 7, it is reasonable to assign the flat band at 2.2 eV to the partially occupied $t_{2\text{g}}$ bands and the slightly dispersive band at 3 eV to the occupied e_{g} bands although the experimental binding energies disagree with those in the calculations. This assignment is also consistent with the experimental result that the 2.2 -eV band shows a greater increase in intensity than the 3 -eV band in the measurement with He I α and He II α , indicating that the 2.2 -eV band has a larger Fe 3d contribution. The discrepancy between the experimental and calculated band structures suggests the difficulty in the theoretical prediction of the electronic properties of the FeBr₂ film. As mentioned in the previous theoretical work,^{30,32} the structural parameters, electron correlation, and spin–orbit interaction strongly affect the calculated electronic structure. These parameters not only influence the Fe 3d bands but also affect Br 4p bands.²⁹ The energy relationship of the lowest bands at \bar{M} and \bar{K} is calculated to be reversed depending on the electron correlation value. The lowest band at \bar{M} is experimentally observed at higher binding energy than that at \bar{K} . In addition, the calculated width of the Fe 3d band is typically more than 0.5 eV, which is not consistent with the experimentally observed nearly flat band. Future theoretical work is required to quantitatively evaluate these parameters and further understand the electronic structure and interaction between the magnetic and electronic properties of the promising vdW magnet, FeBr₂.

CONCLUSIONS

In summary, we have demonstrated the MBE growth of few-layer (0001)-oriented FeBr₂ films on the Bi(111) surface by LEED and ARPES. The sharp LEED pattern with multiple moiré spots and the clear distinction in band structure between the multilayer and monolayer films indicate that the FeBr₂ film is epitaxially grown from the monolayer. The electronic structure of the films is insulating down to the monolayer, where the topmost Fe 3d band is located at 2.2 eV below the Fermi level. The establishment of the high-quality ultrathin FeBr₂ films on Bi(111) with a sharp moiré pattern will

encourage further investigation not only on the magnetic properties of the few-layer FeBr₂ films but also on the physical properties of the interface between the magnetic layers and the Bi(111) surface with spin-polarized metallic states due to strong Rashba-type spin-orbit interaction.⁵¹

AUTHOR INFORMATION

Corresponding Author

Shigemi Terakawa – *Nano-Systems from Ions, Spins and Electrons, Max Planck Institute of Microstructure Physics, Halle 06120, Germany; Department of Chemistry, Graduate School of Science, Kyoto University, Kyoto 606-8502, Japan;*
orcid.org/0000-0001-5790-7234; Email: sterakawa@mpi-halle.mpg.de

Authors

Shinichiro Hatta – *Department of Chemistry, Graduate School of Science, Kyoto University, Kyoto 606-8502, Japan;*
orcid.org/0000-0001-5034-5187

Hiroshi Okuyama – *Department of Chemistry, Graduate School of Science, Kyoto University, Kyoto 606-8502, Japan;*
orcid.org/0000-0002-6031-0612

Tetsuya Aruga – *Department of Chemistry, Graduate School of Science, Kyoto University, Kyoto 606-8502, Japan*

Complete contact information is available at:
<https://pubs.acs.org/10.1021/acs.jpcc.3c02188>

Funding

Open access funded by Max Planck Society.

Notes

The authors declare no competing financial interest.

ACKNOWLEDGMENTS

The present work was financially supported by JSPS KAKENHI (Grant Nos. 19H01825, 20J10847, 21K03432). The authors thank the Supercomputer Center, the Institute for Solid State Physics, the University of Tokyo (Project No. 2023-Ba-0031) for the use of the facilities, and Center for Computational Materials Science, Institute for Materials Research, Tohoku University for the use of MASAMUNE-IMR (Project No. 2212SC0005).

REFERENCES

- (1) Geim, A. K.; Novoselov, K. S. The rise of graphene. *Nat. Mater.* **2007**, *6*, 183–191.
- (2) Castro Neto, A. H.; Guinea, F.; Peres, N. M. R.; Novoselov, K. S.; Geim, A. K. The electronic properties of graphene. *Rev. Mod. Phys.* **2009**, *81*, 109–162.
- (3) Burch, K. S.; Mandrus, D.; Park, J.-G. Magnetism in two-dimensional van der Waals materials. *Nature* **2018**, *563*, 47–52.
- (4) Gong, C.; Zhang, X. Two-dimensional magnetic crystals and emergent heterostructure devices. *Science* **2019**, *363*, No. 706.
- (5) Li, H.; Ruan, S.; Zeng, Y.-J. Intrinsic van der Waals magnetic materials from bulk to the 2D limit: new frontiers of spintronics. *Adv. Mater.* **2019**, *31*, No. 1900065.
- (6) Wang, M. C.; Huang, C. C.; Cheung, C. H.; Chen, C. Y.; Tan, S. G.; Huang, T. W.; Zhao, Y.; Zhao, Y.; Wu, G.; Feng, Y. P.; et al. Prospects and opportunities of 2D van der Waals magnetic systems. *Ann. Phys.* **2020**, *532*, No. 1900452.
- (7) Cortie, D. L.; Causer, G. L.; Rule, K. C.; Fritzsche, H.; Kreuzpaintner, W.; Klose, F. Two-dimensional magnets: forgotten history and recent progress towards spintronic applications. *Adv. Funct. Mater.* **2020**, *30*, No. 1901414.
- (8) Blei, M.; Lado, J. L.; Song, Q.; Dey, D.; Erten, O.; Pardo, V.; Comin, R.; Tongay, S.; Botana, A. S. Synthesis, engineering, and theory of 2D van der Waals magnets. *Appl. Phys. Rev.* **2021**, *8*, No. 021301.
- (9) Wang, Q. H.; Bedoya-Pinto, A.; Blei, M.; Dismukes, A. H.; Hamo, A.; Jenkins, S.; Koperski, M.; Liu, Y.; Sun, Q.-C.; Telford, E. J.; et al. The magnetic genome of two-dimensional van der Waals materials. *ACS Nano* **2022**, *16*, 6960–7079.
- (10) Bora, M.; Deb, P. Magnetic proximity effect in two-dimensional van der Waals heterostructure. *J. Phys. Mater.* **2021**, *4*, No. 034014.
- (11) Tokura, Y.; Yasuda, K.; Tsukazaki, A. Magnetic topological insulators. *Nat. Rev. Phys.* **2019**, *1*, 126–143.
- (12) Kezilebieke, S.; Huda, M. N.; Vaňo, V.; Aapro, M.; Ganguli, S. C.; Silveira, O. J.; Glódzik, S.; Foster, A. S.; Ojanen, T.; Liljeroth, P. Topological superconductivity in a van der Waals heterostructure. *Nature* **2020**, *588*, 424–428.
- (13) Huang, B.; Clark, G.; Navarro-Moratalla, E.; Klein, D. R.; Cheng, R.; Seyler, K. L.; Zhong, D.; Schmidgall, E.; McGuire, M. A.; Cobden, D. H.; et al. Layer-dependent ferromagnetism in a van der Waals crystal down to the monolayer limit. *Nature* **2017**, *546*, 270–273.
- (14) Kim, M.; Kumaravel, P.; Birkbeck, J.; Kuang, W.; Xu, S. G.; Hopkinson, D. G.; Knolle, J.; McClarty, P. A.; Berdyugin, A. I.; Shalom, M. B.; et al. Micromagnetometry of two-dimensional ferromagnets. *Nat. Electron.* **2019**, *2*, 457–463.
- (15) Bedoya-Pinto, A.; Ji, J. R.; Pandeya, A. K.; Gargiani, P.; Valvidares, M.; Sessi, P.; Taylor, J. M.; Radu, F.; Chang, K.; Parkin, S. S. Intrinsic 2D-XY ferromagnetism in a van der Waals monolayer. *Science* **2021**, *374*, 616–620.
- (16) Gong, C.; Li, L.; Li, Z.; Ji, H.; Stern, A.; Xia, Y.; Cao, T.; Bao, W.; Wang, C.; Wang, Y.; et al. Discovery of intrinsic ferromagnetism in two-dimensional van der Waals crystals. *Nature* **2017**, *546*, 265–269.
- (17) Fei, Z.; Huang, B.; Malinowski, P.; Wang, W.; Song, T.; Sanchez, J.; Yao, W.; Xiao, D.; Zhu, X.; May, A. F.; et al. Two-dimensional itinerant ferromagnetism in atomically thin Fe₃GeTe₂. *Nat. Mater.* **2018**, *17*, 778–782.
- (18) McGuire, M. A. Crystal and magnetic structures in layered, transition metal dihalides and trihalides. *Crystals* **2017**, *7*, 121.
- (19) Zhou, X.; Brzostowski, B.; Durajski, A.; Liu, M.; Xiang, J.; Jiang, T.; Wang, Z.; Chen, S.; Li, P.; Zhong, Z.; et al. Atomically thin 1T-FeCl₂ grown by molecular-beam epitaxy. *J. Phys. Chem. C* **2020**, *124*, 9416–9423.
- (20) Cai, S.; Yang, F.; Gao, C. FeCl₂ monolayer on HOPG: Art of growth and momentum filtering effect. *Nanoscale* **2020**, *12*, 16041–16045.
- (21) Jiang, S.; Wang, G.; Deng, H.; Liu, K.; Yang, Q.; Zhao, E.; Zhu, L.; Guo, W.; Yang, J.; Zhang, C.; et al. General synthesis of 2D magnetic transition metal dihalides via trihalide reduction. *ACS Nano* **2023**, *17*, 363–371.
- (22) Liu, H.; Wang, X.; Wu, J.; Chen, Y.; Wan, J.; Wen, R.; Yang, J.; Liu, Y.; Song, Z.; Xie, L. Vapor deposition of magnetic van der Waals NiI₂ crystals. *ACS Nano* **2020**, *14*, 10544–10551.
- (23) Bikaljević, D.; González-Orellana, C.; Peña-Díaz, M.; Steiner, D.; Dreiser, J.; Gargiani, P.; Foerster, M.; Ángel Niño, M.; Aballe, L.; Ruiz-Gomez, S.; et al. Noncollinear magnetic order in two-dimensional NiBr₂ films grown on Au(111). *ACS Nano* **2021**, *15*, 14985–14995.
- (24) Wilkinson, M. K.; Cable, J. W.; Wollan, E. O.; Koehler, W. C. Neutron diffraction investigations of the magnetic ordering in FeBr₂, CoBr₂, FeCl₂, and CoCl₂. *Phys. Rev.* **1959**, *113*, 497–507.
- (25) Fert, A. R.; Carrara, P.; Lanusse, M. C.; Mischler, G.; Redoules, J. P. Transition de phase metamagnétique du bromure ferreux. *J. Phys. Chem. Solids* **1973**, *34*, 223–230.
- (26) Torun, E.; Sahin, H.; Singh, S. K.; Peeters, F. M. Stable half-metallic monolayers of FeCl₂. *Appl. Phys. Lett.* **2015**, *106*, No. 192404.
- (27) Ashton, M.; Gluhovic, D.; Sinnott, S. B.; Guo, J.; Stewart, D. A.; Hennig, R. G. Two-dimensional intrinsic half-metals with large spin gaps. *Nano Lett.* **2017**, *17*, 5251–5257.

- (28) Feng, Y.; Wu, X.; Han, J.; Gao, G. Robust half-metallicities and perfect spin transport properties in 2D transition metal dichlorides. *J. Mater. Chem. C* **2018**, *6*, 4087–4094.
- (29) Kovaleva, E. A.; Melchakova, I.; Mikhaleva, N. S.; Tomilin, F. N.; Ovchinnikov, S. G.; Baek, W.; Pomogaev, V. A.; Avramov, P.; Kuzubov, A. A. The role of strong electron correlations in determination of band structure and charge distribution of transition metal dihalide monolayers. *J. Phys. Chem. Solids* **2019**, *134*, 324–332.
- (30) Botana, A. S.; Norman, M. R. Electronic structure and magnetism of transition metal dihalides: Bulk to monolayer. *Phys. Rev. Mater.* **2019**, *3*, No. 044001.
- (31) Lu, D.; Liu, L.; Ma, Y.; Yang, K.; Wu, H. A unique electronic state in a ferromagnetic semiconductor FeCl₂ monolayer. *J. Mater. Chem. C* **2022**, *10*, 8009–8014.
- (32) Yao, Q.; Li, J.; Liu, Q. Fragile symmetry-protected half metallicity in two-dimensional van der Waals magnets: A case study of monolayer FeCl₂. *Phys. Rev. B* **2021**, *104*, No. 035108.
- (33) Nagao, T.; Sadowski, J. T.; Saito, M.; Yaginuma, S.; Fujikawa, Y.; Kogure, T.; Ohno, T.; Hasegawa, Y.; Hasegawa, S.; Sakurai, T. Nanofilm allotrope and phase transformation of ultrathin Bi film on Si(111)-7×7. *Phys. Rev. Lett.* **2004**, *93*, No. 105501.
- (34) Yaginuma, S.; Nagao, T.; Sadowski, J. T.; Pucci, A.; Fujikawa, Y.; Sakurai, T. Surface pre-melting and surface flattening of Bi nanofilms on Si(111)-7×7. *Surf. Sci.* **2003**, *547*, L877–L881.
- (35) Blöchl, P. E. Projector augmented-wave method. *Phys. Rev. B* **1994**, *50*, No. 17953.
- (36) Kresse, G.; Joubert, D. From ultrasoft pseudopotentials to the projector augmented-wave method. *Phys. Rev. B* **1999**, *59*, No. 1758.
- (37) Kresse, G.; Hafner, J. *Ab initio* molecular dynamics for liquid metals. *Phys. Rev. B* **1993**, *47*, No. 558(R).
- (38) Kresse, G.; Furthmüller, J. Efficient iterative schemes for *ab initio* total-energy calculations using a plane-wave basis set. *Phys. Rev. B* **1996**, *54*, No. 11169.
- (39) Kresse, G.; Furthmüller, J. Efficiency of *ab-initio* total energy calculations for metals and semiconductors using a plane-wave basis set. *Comput. Mater. Sci.* **1996**, *6*, 15–50.
- (40) Klimeš, J.; Bowler, D. R.; Michaelides, A. Van der Waals density functionals applied to solids. *Phys. Rev. B* **2011**, *83*, No. 195131.
- (41) Perdew, J. P.; Burke, K.; Ernzerhof, M. Generalized gradient approximation made simple. *Phys. Rev. Lett.* **1996**, *77*, No. 3865.
- (42) Haberecht, J.; Borrmann, H.; Kniep, R. Refinement of the crystal structure of iron dibromide, FeBr₂. *Z. Kristallogr. - New Cryst. Struct.* **2001**, *216*, 510.
- (43) Momma, K.; Izumi, F. VESTA 3 for three-dimensional visualization of crystal, volumetric and morphology data. *J. Appl. Crystallogr.* **2011**, *44*, 1272–1276.
- (44) Barbieri, A.; Hove, M. A. V. *Symmetrized Automated Tensor Leed (SATLEED) package available from M. A. Van Hove.*
- (45) Pendry, J. B. Reliability factors for LEED calculations. *J. Phys. C: Solid State Phys.* **1980**, *13*, 937–944.
- (46) Yeh, J. J.; Lindau, I. Atomic subshell photoionization cross sections and asymmetry parameters: $1 \leq Z \leq 103$. *At. Data Nucl. Data Tables* **1985**, *32*, 1–155.
- (47) Rusz, J.; Sargolzaei, M. Spin and orbital magnetism of FeBr₂: a density functional theory study. *J. Phys.: Condens. Matter* **2008**, *20*, No. 025217.
- (48) Kundu, A. K.; Liu, Y.; Petrovic, C.; Valla, T. Valence band electronic structure of the van der Waals ferromagnetic insulators: VI₃ and CrI₃. *Sci. Rep.* **2020**, *10*, No. 15602.
- (49) De Vita, A.; Nguyen, T. T. P.; Sant, R.; Pierantozzi, G. M.; Amoroso, D.; Bigi, C.; Polewczyk, V.; Vinai, G.; Nguyen, L. T.; Kong, T.; et al. Influence of orbital character on the ground state electronic properties in the van der Waals transition metal iodides VI₃ and CrI₃. *Nano Lett.* **2022**, *22*, 7034–7041.
- (50) Jiang, W.; Yang, Z.; Li, Y.; Wang, G.; Jing, Q.; Guan, D.; Ma, J.; Zhang, W.; Qian, D. Spin-split valence bands of the ferromagnetic insulator Cr₂Ge₂Te₆ studied by angle-resolved photoemission spectroscopy. *J. Appl. Phys.* **2020**, *127*, No. 023901.
- (51) Koroteev, Y. M.; Bihlmayer, G.; Gayone, J. E.; Chulkov, E. V.; Blügel, S.; Echenique, P. M.; Hofmann, P. Strong spin-orbit splitting on Bi surfaces. *Phys. Rev. Lett.* **2004**, *93*, No. 046403.

Recommended by ACS

Imaging Nucleation and Propagation of Pinned Domains in Few-Layer Fe_{5-x}GeTe₂

Michael Högen, Mete Atatüre, et al.

AUGUST 29, 2023
ACS NANO

READ 

Room-Temperature and Tunable Tunneling Magnetoresistance in Fe₃GaTe₂-Based 2D van der Waals Heterojunctions

Wen Jin, Haixin Chang, et al.

JULY 19, 2023
ACS APPLIED MATERIALS & INTERFACES

READ 

Layered van der Waals Chalcogenides FeAl₂Se₄, MnAl₂S₄, and MnAl₂Se₄: Atomically Thin Triangular Arrangement of Transition-Metal Atoms

Valeriy Yu. Verchenko, Andrei V. Shevelkov, et al.

MAY 02, 2023
INORGANIC CHEMISTRY

READ 

Visualizing the Effect of Oxidation on Magnetic Domain Behavior of Nanoscale Fe₃GeTe₂ for Applications in Spintronics

Yue Li, Charudatta Phatak, et al.

MARCH 10, 2023
ACS APPLIED NANO MATERIALS

READ 

Get More Suggestions >